

Effect of gas blowing nozzle angle on multiphase flow and mass transfer during RH refining process

Jiahao Wang, Peiyuan Ni, Chao Chen, Mikael Ersson, and Ying Li

Cite this article as:

Jiahao Wang, Peiyuan Ni, Chao Chen, Mikael Ersson, and Ying Li, Effect of gas blowing nozzle angle on multiphase flow and mass transfer during RH refining process, *Int. J. Miner. Metall. Mater.*, 30(2023), No. 5, pp. 844-856. <https://doi.org/10.1007/s12613-022-2558-5>

View the article online at [SpringerLink](#) or [IJMMM Webpage](#).

Articles you may be interested in

Yi-hong Li, Yan-ping Bao, Rui Wang, Li-feng Ma, and Jian-sheng Liu, [Modeling study on the flow patterns of gas-liquid flow for fast decarburization during the RH process](#), *Int. J. Miner. Metall. Mater.*, 25(2018), No. 2, pp. 153-163. <https://doi.org/10.1007/s12613-018-1558-y>

Ju-jin Wang, Li-feng Zhang, Gong Cheng, Qiang Ren, and Ying Ren, [Dynamic mass variation and multiphase interaction among steel, slag, lining refractory and nonmetallic inclusions: Laboratory experiments and mathematical prediction](#), *Int. J. Miner. Metall. Mater.*, 28(2021), No. 8, pp. 1298-1308. <https://doi.org/10.1007/s12613-021-2304-4>

Jian-hua Chu and Yan-ping Bao, [Mn evaporation and denitrification behaviors of molten Mn steel in the vacuum refining with slag process](#), *Int. J. Miner. Metall. Mater.*, 28(2021), No. 8, pp. 1288-1297. <https://doi.org/10.1007/s12613-021-2311-5>

Gao-hui Li, Li Zhou, Ling-yun Luo, Xi-ming Wu, and Ning Guo, [Material flow behavior and microstructural evolution during refill friction stir spot welding of alclad 2A12-T4 aluminum alloy](#), *Int. J. Miner. Metall. Mater.*, 28(2021), No. 1, pp. 131-141. <https://doi.org/10.1007/s12613-020-1998-z>

Xing Zhao, Hong-liang Zhao, Li-feng Zhang, and Li-qiang Yang, [Gas-liquid mass transfer and flow phenomena in the Peirce-Smith converter: a water model study](#), *Int. J. Miner. Metall. Mater.*, 25(2018), No. 1, pp. 37-44. <https://doi.org/10.1007/s12613-018-1544-4>

Chao Pan, Xiao-jun Hu, Jian-chao Zheng, Ping Lin, and Kuo-chih Chou, [Effect of calcium content on inclusions during the ladle furnace refining process of AISI 321 stainless steel](#), *Int. J. Miner. Metall. Mater.*, 27(2020), No. 11, pp. 1499-1507. <https://doi.org/10.1007/s12613-020-1981-8>



IJMMM WeChat



QQ author group

Effect of gas blowing nozzle angle on multiphase flow and mass transfer during RH refining process

Jiahao Wang^{1,2)}, Peiyuan Ni^{1,2),✉}, Chao Chen³⁾, Mikael Ersson⁴⁾, and Ying Li^{1,2),✉}

1) Key Laboratory of Ecological Metallurgy of Multi-metal Intergrown Ores of Education Ministry, School of Metallurgy, Northeastern University, Shenyang 110819, China

2) Liaoning Key Laboratory of Metallurgical Sensor Materials and Technology, School of Metallurgy, Northeastern University, Shenyang 110819, China

3) College of Materials Science and Engineering, Taiyuan University of Technology, Taiyuan 030024, China

4) Department of Materials Science and Engineering, KTH Royal Institute of Technology, Stockholm SE-10044, Sweden

(Received: 19 August 2022; revised: 16 September 2022; accepted: 29 September 2022)

Abstract: A three-dimensional mathematical model was developed to investigate the effect of gas blowing nozzle angles on multiphase flow, circulation flow rate, and mixing time during Ruhrstahl-Heraeus (RH) refining process. Also, a water model with a geometric scale of 1:4 from an industrial RH furnace of 260 t was built up, and measurements were carried out to validate the mathematical model. The results show that, with a conventional gas blowing nozzle and the total gas flow rate of 40 L·min⁻¹, the mixing time predicted by the mathematical model agrees well with the measured values. The deviations between the model predictions and the measured values are in the range of about 1.3%–7.3% at the selected three monitoring locations, where the mixing time was defined as the required time when the dimensionless concentration is within 3% deviation from the bath averaged value. In addition, the circulation flow rate was 9 kg·s⁻¹. When the gas blowing nozzle was horizontally rotated by either 30° or 45°, the circulation flow rate was found to be increased by about 15% compared to a conventional nozzle, due to the rotational flow formed in the up-snorkel. Furthermore, the mixing time at the monitoring point 1, 2, and 3 was shortened by around 21.3%, 28.2%, and 12.3%, respectively. With the nozzle angle of 30° and 45°, the averaged residence time of 128 bubbles in liquid was increased by around 33.3%.

Keywords: Ruhrstahl-Heraeus refining; gas blowing nozzle angle; circulation flow rate; mixing time; multiphase flow

1. Introduction

Ruhrstahl-Heraeus, namely RH furnace, is one of the most important refining equipment in steel production, mainly used for some high-quality steel production such as ultra-low carbon steel, electrical steel, bearing steel, pipeline steel, and so on. The structure of a RH furnace is shown in Fig. 1. At present, RH furnace has been developed into multifunctional refining equipment with decarburization, degassing, desulfurization, the removal of inclusions, and the adjustment of steel temperature and compositions.

Mixing time and circulation flow rate are the key characteristics to evaluate the refining efficiency of RH furnace, which are significantly influenced by steel flow behaviors. Due to the limitation of the high steel temperature, a direct investigation on multiphase flow behaviors during a RH refining process is very difficult. Therefore, numerical simulations have been widely used. Initially, the flow phenomena during a RH refining were simulated to be simplified into a single-phase flow [1–6]. Therefore, it cannot properly describe the multi-phase flow phenomena which happen in a real RH reactor. Then, the Eulerian-Lagrangian [7] and Eu-

lerian-Eulerian [8–9] approach were used to simulate the RH refining process. These two methods can generally depict the flow phenomena, which is validated by water model experiments. In above studies, the vacuum chamber and the top surface of the ladle were assumed to be flat, ignoring the existence of top gas or top slag phase. In order to track the interface behavior, a combined discrete phase model (DPM)–volume of fluid (VOF) approach was used to simulate the RH refining process [10–11]. Recently, a new model called the particle-free surface coupled model was used to investigate the argon-steel-slag flow in the vacuum chamber [12], where the size change of gas bubbles was considered. Chen *et al.* [13] and Shao *et al.* [14] established a coupled model of computational fluid dynamics model and population balance model to simulate the multiphase flow during RH refining process. Numerical simulations are usually validated either by water model experiments or by industrial measurements to show its reliability [6,10].

The circulation flow rate and mixing time of a RH refining process depend on many variables. Gas blowing nozzle number is an important factor that affects the circulation flow rate. Generally, an increased number of gas plumes in the up-

✉ Corresponding authors: Peiyuan Ni E-mail: nipeiyuan@smm.neu.edu.cn; Ying Li E-mail: liying@mail.neu.edu.cn

© University of Science and Technology Beijing 2023

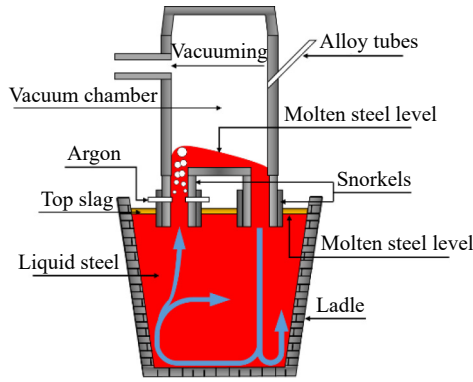


Fig. 1. Schematic diagram of a RH furnace.

snorkel leads to an increased steel volume influenced by the injected gas, and an improved decarburization efficiency [15–17]. However, the circulation flow rate can be decreased when too many nozzles are used [10]. This is due to that each nozzle plume coalesces into a large plume. Gas blowing flow rate is another important factor that affect the circulation flow rate, which has been extensively studied [10,15,18–20]. It was found that the circulation flow rate can be improved by an increased gas flow rate until a ‘saturated level’ was reached. In addition, a lower vacuum chamber pressure can obtain a larger circulation flow rate [21–24]. However, the increase in the gas blowing flow rate is supposed to be more efficient than a low vacuum degree [25]. The multi-leg design and an oval or arched shape of the snorkel cross section was found to be effective to enhance the circulation flow rate [26–30]. Also, a ladle bottom gas injection can shorten the mixing time and improve the refining efficiency [31–34]. However, an excessive gas flow rate can lead to the formation of a slag eye in the ladle and the accelerate erosion on the up-snorkel [35–36].

The circulation flow in a RH system was driven by the gas injection, resulting from the effect of gravity and buoyancy force. The velocities of both liquid and gas in the up-snorkel are mainly in the vertical direction. An additional horizontal velocity may help to improve the mixing of the liquid during passing by the up-snorkel. Li *et al.* [37] investigated the rotational flow phenomena generated by using a mechanical stirring impeller inside the up-snorkel. Water model experiments showed that this technique can increase the circulation flow rate by about 25%. In addition, electromagnetic stirring

method was used to produce a rotational flow in the up-snorkel [38–39]. The results showed that a large circulation flow rate can be obtained with the effect of swirling flow. Qi *et al.* [40] found that the generation of a rotational flow can increase the residence time of bubbles. In addition, Wang *et al.* [41] applied a forward-reverse rotational electromagnetic field to suppress the central vortex formation and to enhance the bubble refinement.

In this work, a new method to produce a rotational flow in the up-snorkel was investigated and it could realize by simply changing the gas blowing nozzle direction. Both water model experiments and numerical simulations were carried out to investigate the multiphase flow behavior in the new design. The effect of the gas blowing nozzle angle on the multiphase flow, mixing time, and circulation flow rate were investigated.

2. Water model experiment

A water model with a geometric scale of 1:4 from a 260 t industrial RH furnace was built up. The dimensions of the water model are given in Table 1. Both the water model and the prototype have 16 nozzles, where 8 nozzles are uniformly distributed on the circumference of an up-snorkel cross section. The specific layout of the nozzles is shown in Fig. 2. The snorkels are immersed 110 mm beneath the free surface in ladle. The similarity of the two systems was guaranteed by the same value of Froude number in Eqs. (1) and (2). The gas flow rate in the water model can be obtained by using Eq. (3) [43], with the value of 40 L·min⁻¹. The pressure in the vacuum chamber is around 97.7 kPa.

The tracer addition position and the monitoring points in the water model are shown in Fig. 3. The stimulus-response approach was used to measure the mixing time in the bath. When the flow in the whole system is fully developed (about 270 s after the start of the gas blowing), 200 mL NaCl saturated solution was poured into the vacuum chamber as the tracer. Then, the changes of the electrical conductivity with time at different locations were measured to determine the bath mixing time.

$$Fr = \frac{\rho_g v_g^2}{gL(\rho_l - \rho_g)} \quad (1)$$

Table 1. Parameters of water model geometry and fluid physical properties

Height of ladle / mm	Diameter of ladle top / mm	Diameter of ladle bottom / mm	Liquid level of ladle / mm	Diameter of snorkel / mm	Length of snorkel / mm	Distance between snorkel / mm
1035	978	929	800	180	412.5	394.5
Diameter of vacuum chamber / mm	Number of nozzles	Diameter of nozzles / mm	Lower layer nozzle height from the bottom of snorkel / mm	Distance between two rows of nozzles / mm	Density of water / (kg·m ⁻³)	Viscosity of water / (10 ⁻³ Pa·s)
574.5	16	2	50	50	1000	1.003
Density of air / (kg·m ⁻³)	Viscosity of air / (10 ⁻⁵ Pa·s)	Density of the saturated NaCl solution / (kg·m ⁻³) [42]	Molar concentration of the saturated NaCl solution / (mol·L ⁻¹) [42]	Interfacial tension of water and air / (N·m ⁻¹)		
1.225	1.79	1197.2	5.326	0.07197		

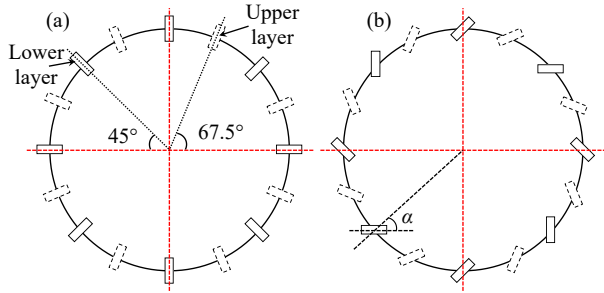


Fig. 2. Top view of nozzle arrangements (a) conventional nozzle and (b) rotated nozzle.

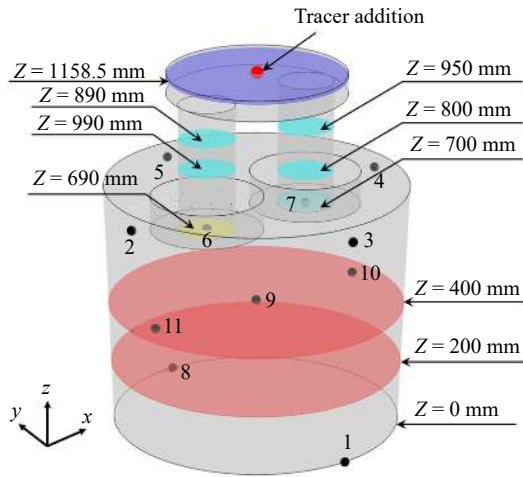


Fig. 3. Locations of monitor points, tracer addition, and different cross sections.

$$\lambda = \frac{L_m}{L_p} \quad (2)$$

$$\frac{Q_m}{Q_p} = \lambda^{2.5} \left(\frac{\rho_{lm}}{\rho_{lp}} \times \frac{\rho_{gp,298K}}{\rho_{gm}} \times \frac{P_m}{P_p} \times \frac{T_p}{T_m} \right)^{0.5} \quad (3)$$

where Fr is the Froude number; ρ_g is gas density, $\text{kg}\cdot\text{m}^{-3}$; ρ_l is liquid density, $\text{kg}\cdot\text{m}^{-3}$; g is the gravitational acceleration rate, $\text{m}\cdot\text{s}^{-2}$; L is a feature length, m ; v_g is gas velocity, $\text{m}\cdot\text{s}^{-1}$; λ is the geometric similarity ratio; Q is gas flow rate, $\text{m}^3\cdot\text{s}^{-1}$; P is gas pressure, Pa ; T is temperature, K ; the subscript m and p represents the water model and prototype, respectively.

3. Mathematical model description

3.1. Model assumptions

The mathematical model was built up based on the following assumptions: (1) Water and air are incompressible Newtonian fluids. (2) The heat and mass transfer between the gas and liquid phases were not considered, and the two-phase flow was assumed to be an isothermal flow. (3) Both the top slag in the ladle and the gas phase in the vacuum chamber were not considered. The liquid surface at the top of both the ladle and the vacuum chamber were assumed to be flat. (4) The gas bubble shape was assumed to be spherical, and their expansion, coalescence and breaking up were not considered. (5) A two-way coupling between water and air bubbles was used.

3.2. Governing equations

The liquid flow field was obtained by solving the continuity equation, momentum equation, and turbulence model equations, as follows [44]:

Continuity equation

$$\frac{\partial \rho_l \mathbf{u}}{\partial t} + \nabla \cdot (\rho_l \mathbf{u}) = 0 \quad (4)$$

Momentum equation

$$\frac{\partial (\rho_l \mathbf{u})}{\partial t} + \nabla \cdot (\rho_l \mathbf{u} \mathbf{u}) = -\nabla P + \nabla \cdot [\mu_{\text{eff}} (\nabla \mathbf{u} + (\nabla \mathbf{u})^T)] + \mathbf{F} + \rho_l \mathbf{g} \quad (5)$$

where \mathbf{u} is liquid velocity, $\text{m}\cdot\text{s}^{-1}$; μ_{eff} is effective viscosity, $\text{Pa}\cdot\text{s}$, which is the sum of laminar viscosity (μ_l) and turbulence viscosity (μ_t); \mathbf{F} is the momentum transfer term exerted by the discrete phase, $\text{N}\cdot\text{m}^{-3}$; \mathbf{g} is the gravitational acceleration rate, $\text{m}\cdot\text{s}^{-2}$.

Turbulent properties of the flow field were solved by using standard k - ε turbulence model. The turbulence viscosity is related to the turbulent kinetic energy k ($\text{m}^2\cdot\text{s}^{-2}$) and the dissipation rate ε ($\text{m}^2\cdot\text{s}^{-3}$) as follows [44]:

$$\mu_t = \rho_l C_\mu \frac{k^2}{\varepsilon} \quad (6)$$

where k and ε can be obtained by solving the following equations [44]:

$$\rho_l \frac{\partial k}{\partial t} + \rho_l \mathbf{u} \cdot \nabla k = \nabla \cdot \left[\left(\mu_l + \frac{\mu_t}{\sigma_k} \right) \nabla k \right] + P_k - \rho_l \varepsilon \quad (7)$$

$$\rho_l \frac{\partial \varepsilon}{\partial t} + \rho_l \mathbf{u} \cdot \nabla \varepsilon = \nabla \cdot \left[\left(\mu_l + \frac{\mu_t}{\sigma_\varepsilon} \right) \nabla \varepsilon \right] + C_{\varepsilon 1} \frac{\varepsilon}{k} P_k - C_{\varepsilon 2} \rho_l \frac{\varepsilon^2}{k} \quad (8)$$

where C_μ , $C_{\varepsilon 1}$, $C_{\varepsilon 2}$, σ_k , and σ_ε are the constants in the turbulence model, with the value of 0.09, 1.44, 1.92, 1.0, and 1.3, respectively [44–45]. The production rate of turbulence kinetic energy P_k is expressed as follows [44]:

$$P_k = \mu_t [\nabla \mathbf{u} : (\nabla \mathbf{u} + (\nabla \mathbf{u})^T)] \quad (9)$$

3.3. Discrete phase model

Air gas is injected into the liquid through the nozzles. The movement of air bubbles can be obtained by solving the following equation [46]:

$$\frac{d\mathbf{x}_p}{dt} = \mathbf{v}_b \quad (10)$$

where \mathbf{x}_p is the bubble position and \mathbf{v}_b is the bubble velocity. The velocity of air bubbles can be computed by the following equation:

$$\frac{d(m_b \mathbf{v}_b)}{dt} = \vec{F}_D + \vec{F}_L + \vec{F}_{VM} + \vec{F}_P + \vec{F}_G + \vec{F}_B \quad (11)$$

where m_b is the mass of bubbles, \vec{F}_D is the drag force, \vec{F}_L is the lift force, \vec{F}_{VM} is the virtual mass force, \vec{F}_P is the pressure gradient force, \vec{F}_G and \vec{F}_B are the gravity and buoyancy force, respectively. These forces are usually considered to investigate the circulation flow rate and mixing time in a RH refining process [10,47].

3.3.1. Drag force

The drag force plays a decisive role in the momentum

transfer between the gas and liquid phase. It can be expressed by the following equation [46]:

$$\vec{F}_D = \frac{m_b(\mathbf{u} - \mathbf{v}_b)}{\tau_b} \quad (12)$$

where τ_b is the particle relaxation time, which can be calculated by the following equation [46]:

$$\tau_b = \frac{4\rho_g d_b^2}{3\mu_l C_D Re_b} \quad (13)$$

where d_b is bubble diameter, Re_b is the Reynolds number of air bubbles, C_D is the drag coefficient, where Schiller and Naumann's [48] drag law was used to calculate this value as follows:

$$C_D = \begin{cases} \frac{24}{Re_b} (1 + 0.15 Re_b^{0.687}) & Re_b \leq 1000 \\ 0.44 & Re_b > 1000 \end{cases} \quad (14)$$

$$Re_b = \frac{\rho_l |\mathbf{u} - \mathbf{v}_b| d_b}{\mu_l} \quad (15)$$

The bubble diameter was calculated through the empirical formula derived by Sano *et al.* [49] as follows:

$$d_b = 0.091 \left(\frac{\sigma_{gl}}{\rho_l} \right)^{0.5} v_{b,0}^{0.44} \quad (16)$$

where σ_{gl} is the surface tension between air and water, $N \cdot m^{-1}$; $v_{b,0}$ is the initial bubble velocity at the entrance which can be calculated by the following equation:

$$v_{b,0} = \frac{Q}{A_{nozzle}} \quad (17)$$

where A_{nozzle} is the total area of all the blowing nozzles, m^2 .

3.3.2. Lift force

The Saffman lift force can be expressed by the following equation [46]:

$$\vec{F}_L = 6.46 r_b^2 L_v \sqrt{\mu_l \rho_l \frac{|\mathbf{u} - \mathbf{v}_b|}{|L_v|}} \quad (18)$$

where r_b is the radius of the bubble, m ; L_v is relative velocity gradient, which is computed by the following equation [46]:

$$L_v = (\mathbf{u} - \mathbf{v}_b) \times [\nabla \times (\mathbf{u} - \mathbf{v}_b)] \quad (19)$$

3.3.3. Virtual mass force

The virtual mass force is proportional to the relative acceleration of the discrete phase, which can be calculated by the following equation [46]:

$$\vec{F}_{VM} = \frac{\pi d_b^3 \rho_l}{12} \frac{d(\mathbf{u} - \mathbf{v}_b)}{dt} \quad (20)$$

3.3.4. Pressure gradient force

The pressure gradient force can be expressed by the following equation [46]:

$$\vec{F}_p = \frac{\pi d_b^3 \rho_l}{6} \left(\frac{\partial \mathbf{u}}{\partial t} + \mathbf{u} \cdot \nabla \mathbf{u} \right) \quad (21)$$

3.3.5. Gravity and buoyancy force

The gravity and buoyancy forces are given by the following equation [46]:

$$\vec{F}_G + \vec{F}_B = m_b \mathbf{g} \frac{(\rho_g - \rho_l)}{\rho_g} \quad (22)$$

3.4. Turbulent dispersion model

In order to consider the effect of turbulent fluctuations on bubble motion, the DRW (Discrete random walk) model was used. The instantaneous velocity can be expressed by the following equation:

$$\mathbf{u} = \bar{\mathbf{u}} + \hat{\mathbf{u}} \quad (23)$$

where $\bar{\mathbf{u}}$ is the averaged velocity of the continuous phase, $\hat{\mathbf{u}}$ is velocity fluctuation component, which is expressed as follows:

$$\hat{\mathbf{u}} = \zeta \sqrt{\frac{2k}{3}} \quad (24)$$

where ζ is a zero mean, which has a unit variance and normally distributed random number.

3.5. Tracer transport

Tracer transport was solved by using the following equation [44]:

$$\frac{\partial C}{\partial t} + \nabla \times (\mathbf{u}C) = \nabla \times [D_{eff} \nabla C] \quad (25)$$

where C is tracer concentration; D_{eff} is effective diffusion coefficient, $m^2 \cdot s^{-1}$, which is the sum of molecule diffusion coefficient (D_0) and turbulent diffusion coefficient (D_t). D_0 value is $0.551 \times 10^{-9} m^2 \cdot s^{-1}$ for NaCl solution at 25°C [50]. D_t can be expressed as the following equation:

$$D_t = \frac{\mu_t}{\rho S c_t} \quad (26)$$

where $S c_t$ is the turbulent Schmidt number, which is equal to 1 in this study.

3.6. Boundary condition and initial condition

A constant velocity was used as the inlet condition for gas blowing. The vacuum chamber pressure is fixed at 97.7 kPa. A non-slip wall boundary condition was used. A reflect boundary condition was used for bubbles once they touch a wall, and they escaped from the calculation domain after they pass by the liquid surface in the vacuum chamber. It was considered to be a fully developed flow at 270 s after gas blowing, which can be seen from the velocity changes at monitoring positions in Fig. 4. Then, 200 mL tracer was released at the same location as that in water model experiment to investigate its transport and the bath mixing behavior.

3.7. Numerical procedure

The numerical model was solved by the commercial software COMSOL Multiphysics 5.6. The mesh with 550,000 grid number was used, as shown in Fig. 5. A fine grid with the size of 1 mm was used at the gas blowing inlet area. The separated constant (Newton) nonlinear method in COMSOL Multiphysics was used to treat non-linear equations. The backward difference formula was firstly used to deal with the convection term. Then, the generalized-alpha method was further used to obtain the final solution. These two methods are all second order scheme. The initial time step was set to 0.0001 s, and the maximum step size was 0.02 s. The conver-

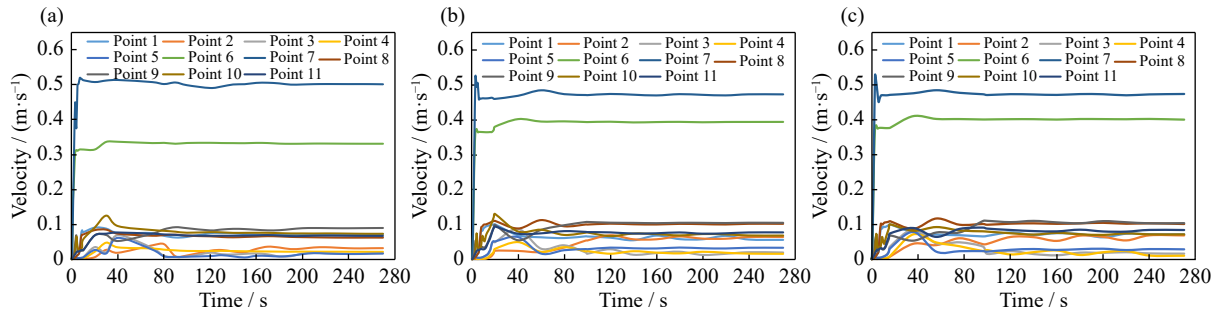


Fig. 4. Predicted velocity changes at monitoring points for different nozzle angles: (a) 0°; (b) 30°; (c) 45°.

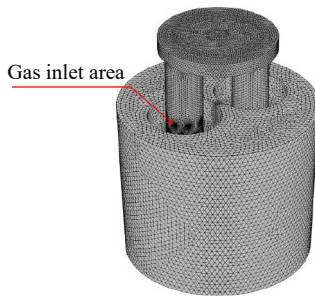


Fig. 5. Grid configuration of the RH model.

gence criteria were as follows: the residuals of all dependent variables were smaller than 1×10^{-3} .

4. Results and discussion

4.1. Model validation

Experimental measurements and numerical simulation were carried out to investigate the mixing time in the RH water model with a conventional nozzle. The mixing time measurements were repeated 10 times to obtain the mean value. Fig. 6 shows the comparison between the model predictions and the measured values. It can be seen from that the deviations at point 1, 2, and 3 were 7.3%, 1.3%, and 7.3%, respectively. Here, the mixing time was defined as the time when a dimensionless concentration was within 3% deviation from the averaged value. With a 5% deviation standard, the mixing time deviations at point 1, 2, and 3 were 15.3%, 4.0%, and 3.1%, respectively. Therefore, the model can generally catch the mixing behavior inside the bath. In the following, the 3% deviation criterion was used to evaluate the bath mixing time.

4.2. Effect of rotated gas blowing nozzle on RH multiphase flow

4.2.1. Mixing time and circulation flow rate

Fig. 7 shows the mixing times at point 1, 2, and 3 under different nozzle blowing angles. It can be seen from that the mixing time at each monitoring point was decreased after either 30° or 45° rotated nozzle. Specifically, when the nozzle rotated from a conventional 0° to 30°, the mixing time at monitoring point 1, 2, and 3 was shortened by 16.2, 24.7, and 9.3 s, respectively, which corresponds to a decrease of 21.3%, 28.2%, and 12.3%. Therefore, a rotated nozzle can effectively reduce the mixing time. With the nozzle angle

changed from 30° to 45°, the mixing time change is very small, as shown in Fig. 7(d).

In order to have a good observation on the mass transfer behavior induced by different nozzle angles, tracer was added at the lower part of the up-snorkel ($Z = 690$ mm cross section as shown in Fig. 3). Fig. 8 shows the variation of tracer concentration with time in the snorkels and the vacuum chamber under different nozzle angles. Compared to a conventional nozzle angle with 0°, the high tracer concentration region seems to move faster towards the down-snorkel when both 30° and 40° rotated nozzles were used. Furthermore, the tracer concentration is more uniform on the cross section of the up-snorkel.

The mixing time and the refining efficiency are related to the circulation flow rate, which can be calculated by using the following equation:

$$R = \rho_l \times \int_{A_0} u_i dA_i \quad (27)$$

where R is the circulation flow rate, $\text{kg} \cdot \text{s}^{-1}$; u_i is the velocity perpendicular to the snorkel cross section, $\text{m} \cdot \text{s}^{-1}$; A_i is each grid area on the cross section, m^2 ; A_0 is the cross-section area, m^2 .

The cross-section of the down-snorkel, located at 700 mm above the bottom of the ladle as shown in Fig. 3, was selected to calculate the circulation flow rate. Fig. 9 shows the calculated values of the circulation flow rate under different nozzle angles. It can be seen that the circulation flow rate increases from 9 to $10.3 \text{ kg} \cdot \text{s}^{-1}$ when the nozzle angle increases from 0° to 30°. With a further increase to 45°, the circulation flow rate increases by only $0.1 \text{ kg} \cdot \text{s}^{-1}$. Therefore, the rotated nozzle injection can increase the circulation flow rate during RH refining. This also explains the faster movement of the high tracer concentration region in the vacuum chamber as shown in Fig. 8.

4.2.2. Flow phenomena in RH furnace

In order to better understand the reason for a high circulation flow rate and a low mixing time, flow phenomena under different nozzle conditions were studied. Fig. 10 shows the streamline of the liquid flow under different nozzle angles. It can be seen that the vertical movement of liquid was observed when a conventional nozzle was used, while a rotational movement was found for both 30° and 45°. This means that the gas momentum provides the force to produce a rotational liquid flow in the up-snorkel. Due to the symmetrical setup of the conventional nozzles, such phenomena were not produced. Fig. 11 shows the velocity distribution on the ver-

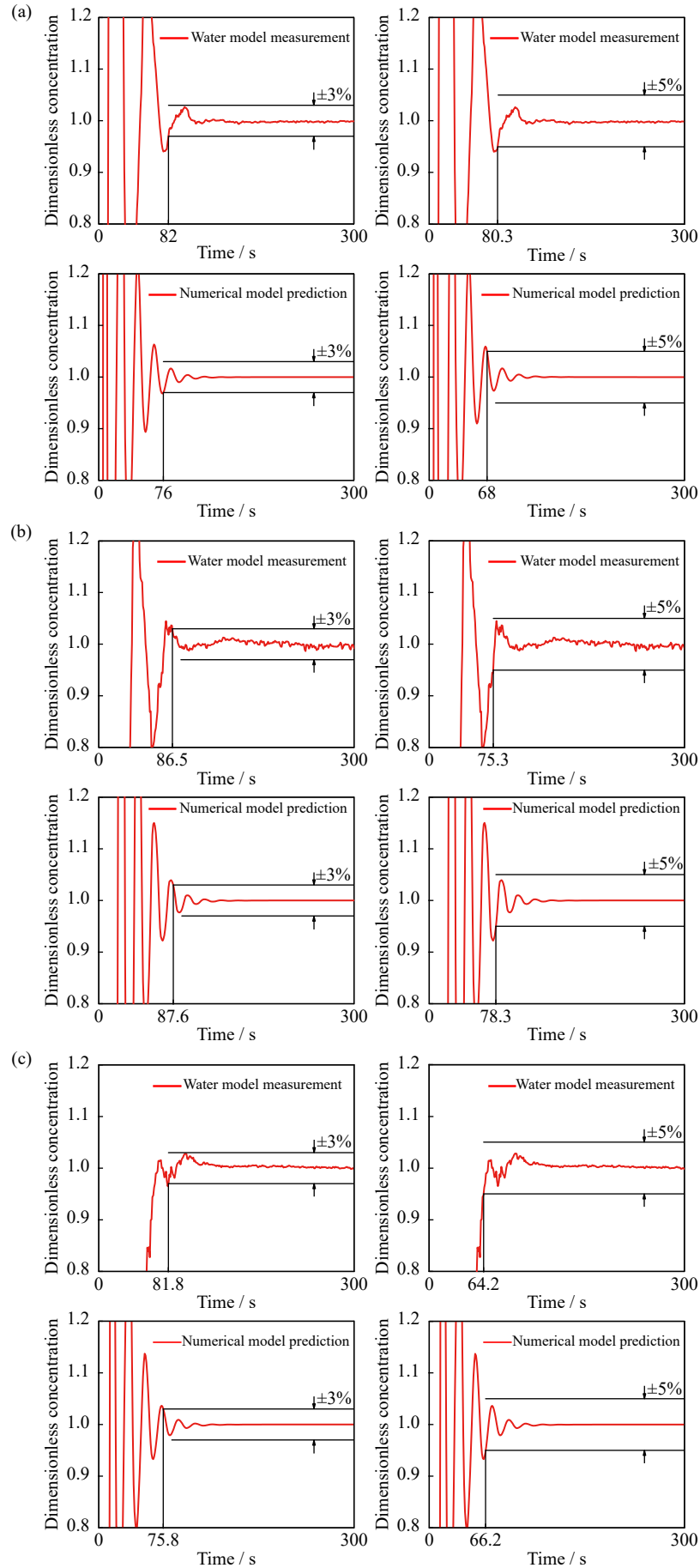


Fig. 6. Comparison of predicted and measured concentration change: (a) point 1; (b) point 2; (c) point 3.

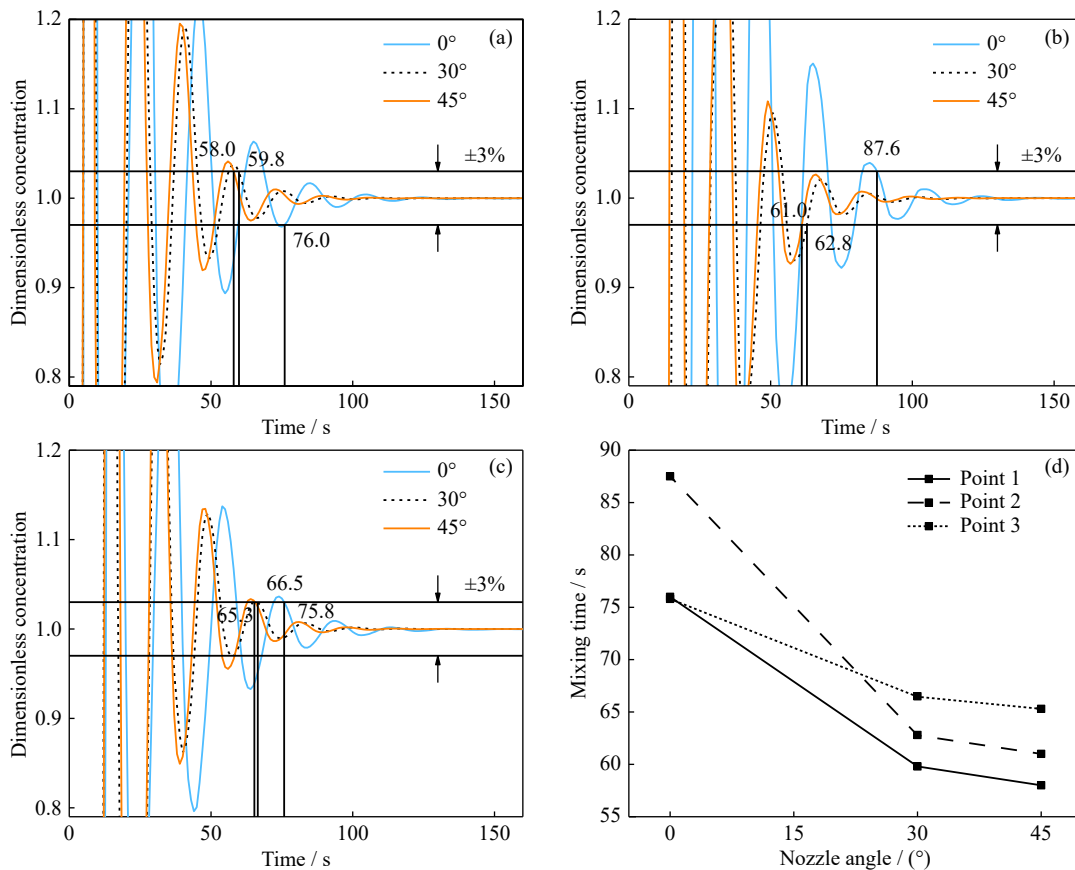


Fig. 7. Effect of nozzle angle on predicted concentration change and mixing time: (a) point 1; (b) point 2; (c) point 3; (d) mixing time at different points and nozzle angles.

tical middle plane of the whole system. As can be seen, the liquid flow velocity in the up-snorkel significantly increased and the velocity distribution became more uniform when 30° and 45° rotated nozzle were used. With a conventional 0°, the gas moves upwards along the wall of the up-snorkel. Therefore, its influence region on liquid is relatively smaller. In addition, with both 30° and 45° rotated nozzle, the liquid velocity in the down-snorkel was also increased. This can also explain the obtained high circulation flow rate in Fig. 9.

To describe the bubble behavior in the RH system intuitively, Fig. 12 shows the trajectories and residence time of the bubbles under different nozzle angles. When the nozzle is not rotated, air bubbles move vertically into the vacuum chamber; when the nozzle was rotated, gas bubbles obtain a rotational movement and move upwards under the action of buoyancy effect. This can be clearly seen from Fig. 12(b) and (c). Under the effect of the considered force in Eq. (11), the spirally rising bubbles lead to the molten steel generating a rotational flow as shown in Fig. 10. In addition, the rotational flow makes bubbles moving towards the up-snorkel center. The average residence time of bubbles can be calculated using the following equation:

$$\bar{t}_b = \frac{\sum_{i=1}^{i=n_b} t_{b,i}}{n_b} \quad (28)$$

where $t_{b,i}$ is the residence time of a bubble, \bar{t}_b is the average

residence time of bubbles, and n_b is the number of bubbles (with the value of 128 in this work). The average residence time is about 0.6 s in the conventional case. When the nozzle rotates 30° and 45°, the average residence time can reach around 0.8 s. In addition, the bubble trajectory length increases in the rotated nozzle cases. These should be beneficial for the refining process that happens at the bubble/steel interface.

In order to clearly understand the flow characteristics in the up-snorkel, Fig. 13 shows the velocity distribution on different cross sections of the up-snorkel under different nozzle angles. For the conventional nozzle case (Fig. 13(a)), the high velocity region was located at the near wall region, and the velocity is very small with the value of about 0.1 m·s⁻¹ in the center region. After the nozzle is horizontally rotated, the fluid in the up-snorkel has formed a good rotational flow. The tangential velocity distribution and its magnitude under different nozzle angles are similar. At the near wall region, the tangential velocity can reach 0.5 m·s⁻¹ as shown in Fig. 13(d)–(f). For the vertical velocity, it can be seen from Fig. 13(g)–(i) that a low velocity region was located at the snorkel center when a conventional nozzle was used. The velocity characteristics on the cross section at a top location can be found from Fig. 13(j)–(r). Generally, it can be seen that a high velocity region is still located at the near wall region for the conventional nozzle case, while it moves towards the snorkel center for rotated nozzle cases. The tangential velocity in Fig. 13(n)–(o) becomes more uniform compared to

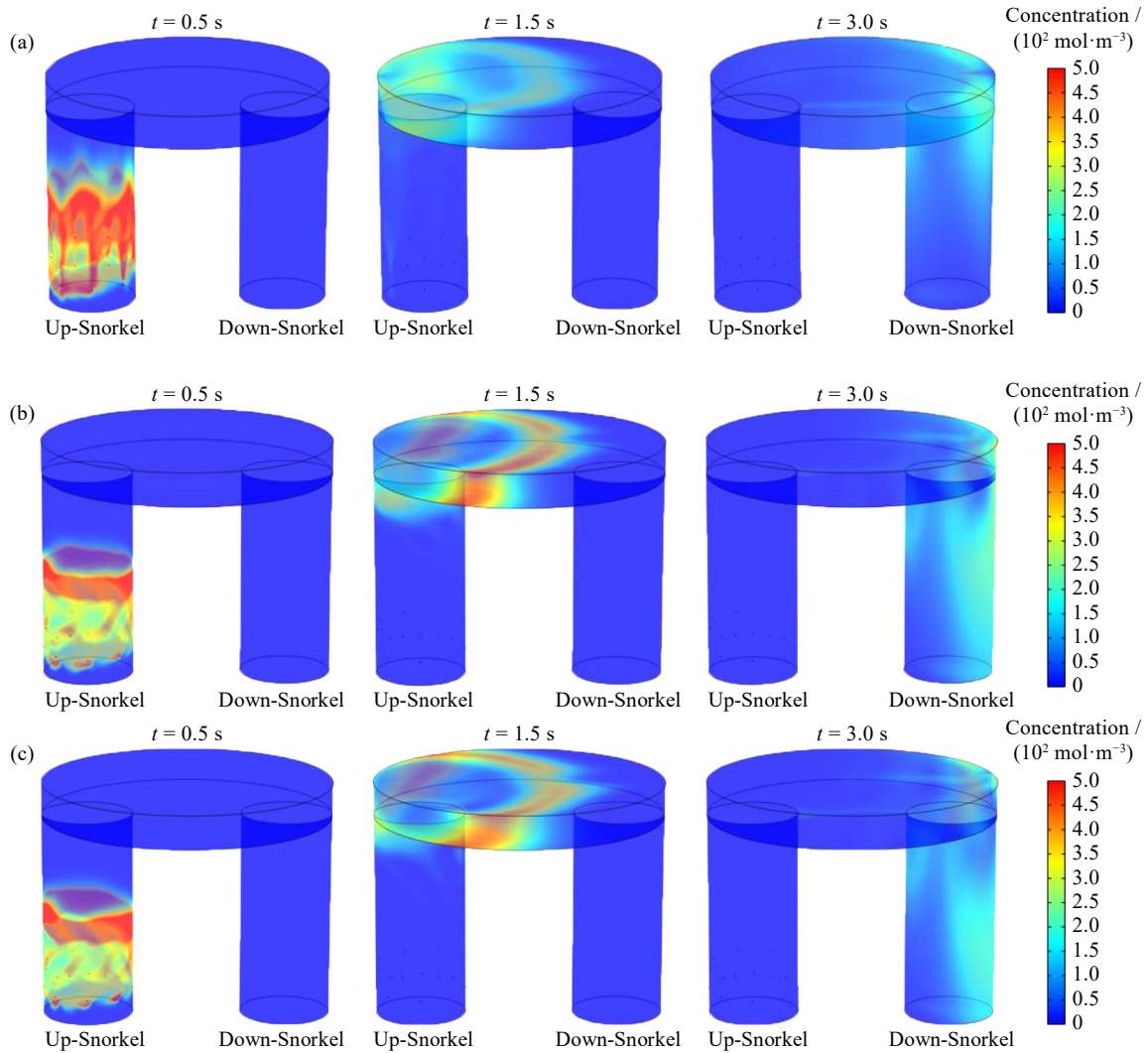


Fig. 8. Movement of the high tracer concentration region in the snorkels and vacuum chamber for different nozzle angles and times: (a) 0°; (b) 30°; (c) 45°.

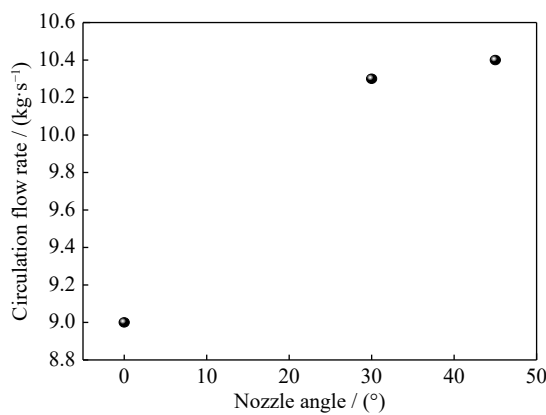


Fig. 9. Effect of nozzle angles on circulation flow rate.

that of Fig. 13(e)–(f). For the vertical velocity, the near wall region shows a low value in Fig. 13(p)–(r) compared to that of Fig. 13(g)–(i). This is attributed to the gas plume moving towards the center region during it passing through the up-snorkel. Therefore, the rotated nozzle design significantly changed the flow behavior in the up-snorkel.

Fig. 14 shows the distributions of the velocity and turbu-

lent kinetic energy on the cross section of the vacuum chamber. It can be seen from Fig. 14(a)–(c) that a symmetrical distribution along the Line 1 was observed for the conventional nozzle case. However, the velocity did not show a symmetrical distribution for the rotated nozzle cases. This is due to the rotational direction of the flow in the up-snorkel. Fig. 14 (d)–(f) shows the turbulent kinetic energy distribution on the cross section. Among the three cases, the highest turbulent kinetic energy was obtained when a conventional nozzle was used. With a rotated nozzle angle, a general uniform total turbulent kinetic energy distribution can be obtained, and the high turbulent kinetic energy region enlarged as shown in Fig. 14(d)–(f).

Fig. 15 shows the velocity distribution on different cross sections of the ladle under different nozzle angles. With a conventional nozzle, the velocity distribution on the ladle cross section shows a symmetrical distribution along the horizontal central line as shown in Fig. 15. However, the distribution is no longer symmetrical in the rotated nozzle cases. Due to the rotational flow in the up-snorkel, the velocity in the vacuum chamber was changed, as shown Fig. 14(a)–(c).

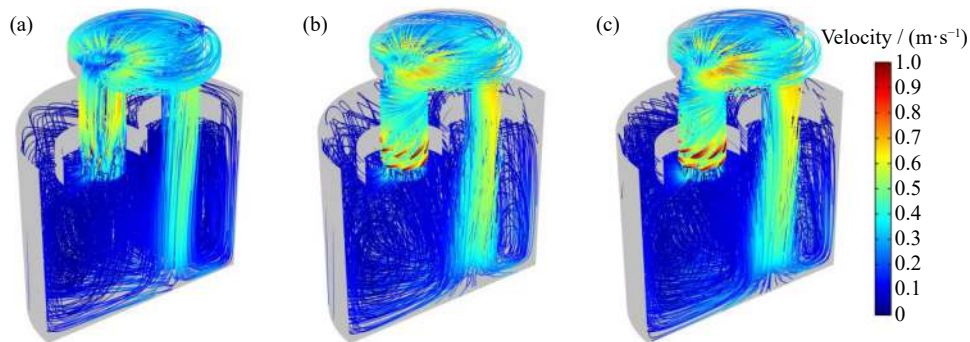


Fig. 10. Streamline of liquid flow under different nozzle angles: (a) 0°; (b) 30°; (c) 45°.

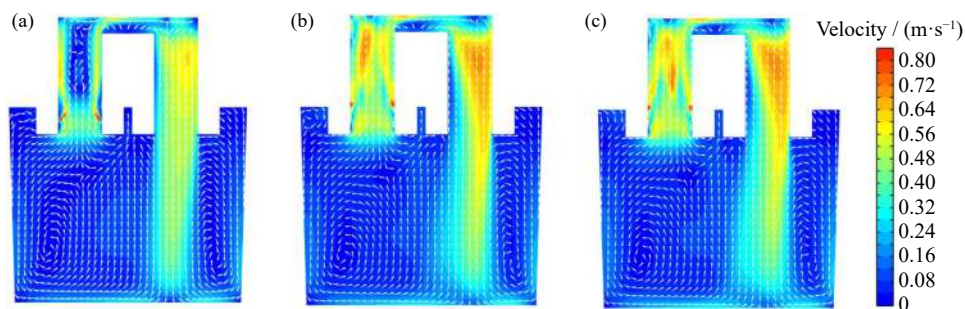


Fig. 11. Velocity distribution on the vertical middle plane of the RH reactor under different nozzle angles: (a) 0°; (b) 30°; (c) 45°.

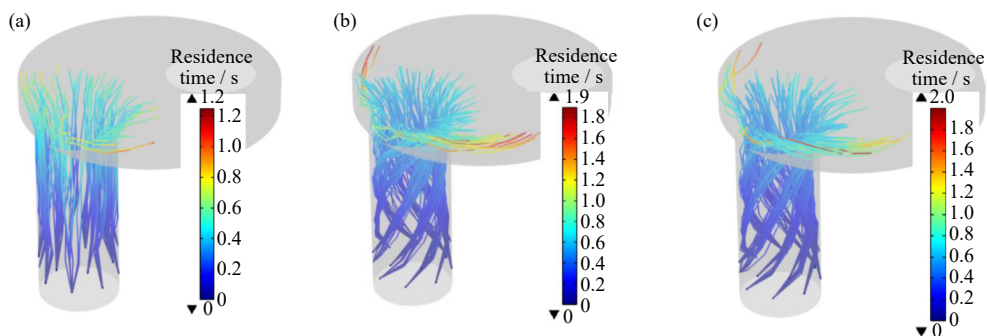


Fig. 12. Trajectories and residence time of the bubbles: (a) 0°; (b) 30°; (c) 45°.

This directly affects the flow behavior inside the down-snorkel and ladle. In addition, the velocity inside the ladle was large when a rotated nozzle angle was used. This is especially true for the near-wall region, and the velocity can reach $0.24 \text{ m}\cdot\text{s}^{-1}$ on the cross section of $Z = 200 \text{ mm}$, with an increase of 20%.

Fig. 16 shows the predicted turbulent kinetic energy distribution on the $Z = 400 \text{ mm}$ plane of the ladle under different nozzle angles. With the rotated nozzles, a larger turbulent kinetic energy was found in the ladle, the maximum magnitude increased from 0.008 (conventional case) to $0.011 \text{ m}^2\cdot\text{s}^{-2}$ (rotated case) compared to the conventional nozzle case, resulting in a more efficient mixing inside the ladle as well as a reduced mixing time as predicted previously.

5. Conclusions

Water model experiment and numerical simulation were carried out to investigate the effect of gas blowing nozzle angle on the mixing time, circulation flow rate, and fluid flow

during RH refining process. The following conclusions were obtained:

(1) The numerical model predictions generally agree well with the measured values, which illustrates its reliability to describe the multiphase flow process in RH refining.

(2) With a rotated nozzle angle of 30° and 45° , the circulation flow rate increased by 14.4% and 15.6%, respectively, compared to a conventional nozzle. Furthermore, the mixing time at monitoring point 1, 2, and 3 were shortened by 21.3%, 28.2%, and 12.3%, respectively.

(3) When 30° and 45° rotated nozzles were used, a rotational movement of liquid was obtained. The liquid flow velocity in the snorkel was significantly increased and the velocity distribution is more uniform in the up-snorkel. The velocity inside the ladle increased especially at the near-wall region.

(4) The residence time of bubbles was increased by a rotated gas blowing nozzle, which was extended by around 33.3% for the nozzle angle of both 30° and 45° of 128 bubbles.

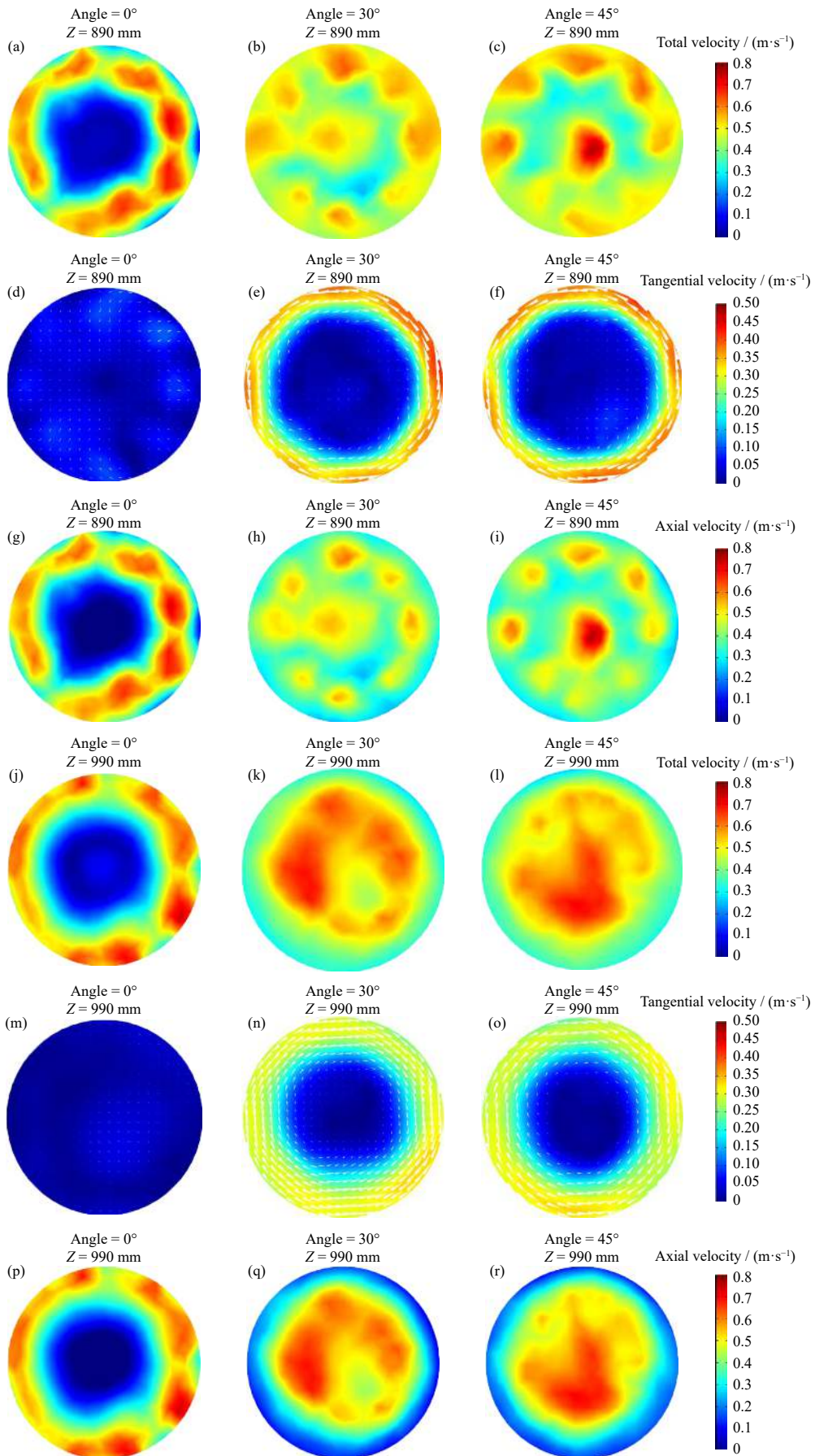


Fig. 13. Velocity distribution on different sections of the up-snorkel under different nozzle angles: (a–c) total velocity at $Z = 890$ mm; (d–f) tangential velocity at $Z = 890$ mm; (g–i) axial velocity at $Z = 890$ mm; (j–l) total velocity at $Z = 990$ mm; (m–o) tangential velocity at $Z = 990$ mm; (p–r) axial velocity at $Z = 990$ mm.

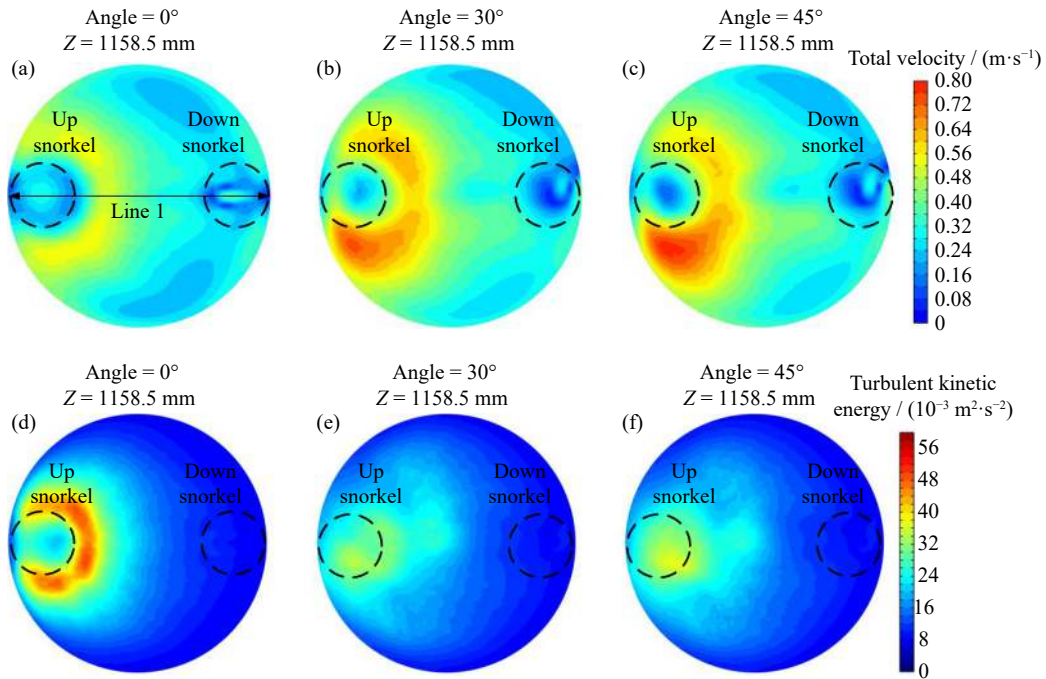


Fig. 14. Predicted properties of the flow field in the vacuum chamber: (a–c) total velocity; (d–f) turbulent kinetic energy.

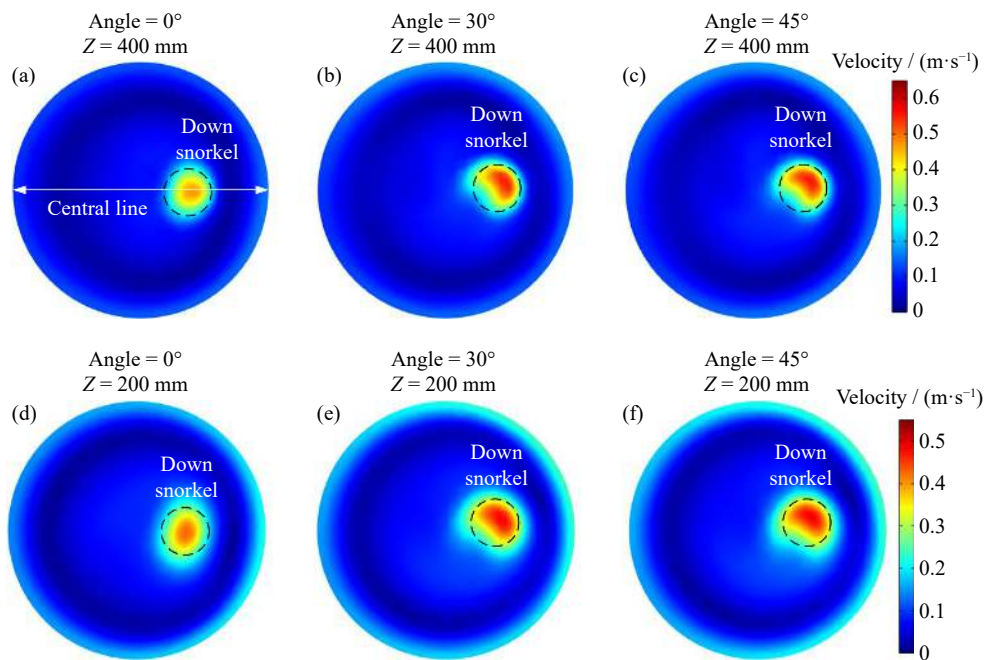


Fig. 15. Distribution of velocity on different cross sections of the ladle under different nozzle angles: (a–c) $Z = 400$ mm; (d–f) $Z = 200$ mm.

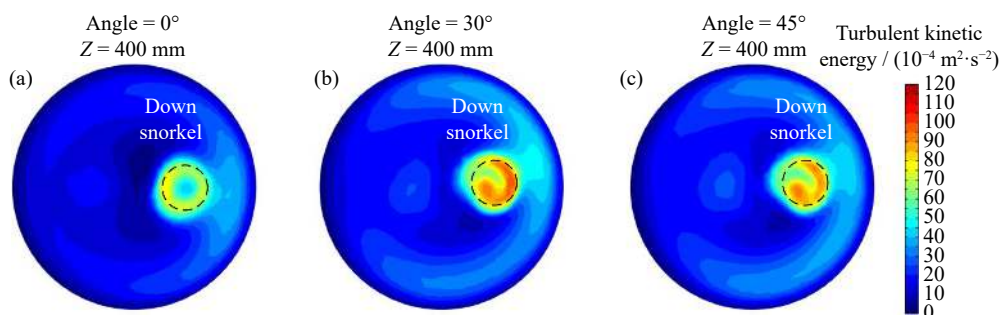


Fig. 16. Distribution of turbulent kinetic energy on the ladle cross section under different nozzle angles: (a) 0°; (b) 30°; (c) 45°.

Acknowledgements

This work was financially supported by the National Natural Science Foundation of China (No. 51704062) and the Fundamental Research Funds for the Central Universities, China (No. N2025019). Jiahao Wang wishes to thank the comments and discussions on the mathematical model from Dr. Xiaobin Zhou from Anhui University of Technology, China.

Conflict of Interest

On behalf of all authors, the corresponding author states that there is no conflict of interest.

References

- [1] K. Nakanishi, J. Szekely, and C.W. Chang, Experimental and theoretical investigation of mixing phenomena in the RH-vacuum process, *Ironmaking Steelmaking*, 2(1975), No. 2, p. 115.
- [2] K. Shirabe and J. Szekely, A mathematical model of fluid flow and inclusion coalescence in the RH vacuum degassing system, *ISIJ Int.*, 23(1983), No. 6, p. 465.
- [3] R. Tsujino, J. Nakashima, M. Hirai, and I. Sawada, Numerical analysis of molten steel flow in ladle of RH process, *ISIJ Int.*, 29(1989), No. 7, p. 589.
- [4] Y. Kato, H. Nakato, T. Fujii, S. Ohmiya, and S. Takatori, Fluid flow in ladle and its effect on decarburization rate in RH degasser, *ISIJ Int.*, 33(1993), No. 10, p. 1088.
- [5] F. Ahrenhold and W. Pluschke, Mixing phenomena inside the ladle during RH decarburization of steel melts, *Steel Res.*, 70(1999), No. 8-9, p. 314.
- [6] S.K. Ajmani, S.K. Dash, S. Chandra, and C. Bhanu, Mixing evaluation in the RH process using mathematical modelling, *ISIJ Int.*, 44(2004), No. 1, p. 82.
- [7] P.A. Kishan and S.K. Dash, Prediction of circulation flow rate in the RH degasser using discrete phase particle modeling, *ISIJ Int.*, 49(2009), No. 4, p. 495.
- [8] J.H. Wei and H.T. Hu, Mathematical modelling of molten steel flow process in a whole RH degasser during the vacuum circulation refining process: Mathematical model of the flow, *Steel Res. Int.*, 77(2006), No. 1, p. 32.
- [9] J.H. Wei and H.T. Hu, Mathematical modelling of molten steel flow process in a whole RH degasser during the vacuum circulation refining process: Application of the model and results, *Steel Res. Int.*, 77(2006), No. 2, p. 91.
- [10] H.T. Ling, F. Li, L.F. Zhang, and A.N. Conejo, Investigation on the effect of nozzle number on the recirculation rate and mixing time in the RH process using VOF+DPM model, *Metall. Mater. Trans. B*, 47(2016), No. 3, p. 1950.
- [11] G.J. Chen, S.P. He, and Y.G. Li, Investigation of the air-argon-steel-slag flow in an industrial RH reactor with VOF-DPM coupled model, *Metall. Mater. Trans. B*, 48(2017), No. 4, p. 2176.
- [12] B. Wang, B.H. Zhu, and B. Zhang, Numerical simulation of gas-steel-slag multiphase flow in the vacuum chamber of the RH degasser, *JOM*, 73(2021), No. 10, p. 2920.
- [13] G.J. Chen and S.P. He, Hydrodynamic modeling of two-phase flow in the industrial Ruhrstahl-Heraeus degasser: Effect of bubble expansion models, *Metall. Mater. Trans. B*, 53(2022), No. 1, p. 208.
- [14] P. Shao, S. Liu, and X. Miao, CFD-PBM simulation of bubble coalescence and breakup in top blown-rotary agitated reactor, *J. Iron Steel Res. Int.*, 29(2022), No. 2, p. 223.
- [15] Y.G. Park, K.W. Yi, and S.B. Ahn, The effect of operating parameters and dimensions of the RH system on melt circulation using numerical calculations, *ISIJ Int.*, 41(2001), No. 5, p. 403.
- [16] R.K. Hanna, T. Jones, R. Blake, and M. Millman, Water modeling to aid improvement of degasser performance for production of ultralow carbon interstitial free steels, *Ironmaking Steelmaking*, 21(1994), p. 37.
- [17] C.W. Li, G.G. Cheng, X.H. Wang, G.S. Zhu, and A.M. Cui, Mathematical model of RH blow argon mode affecting: Decarburization rate in ultra-low carbon steel refining, *J. Iron Steel Res. Int.*, 19(2012), No. 5, p. 23.
- [18] L.C. Trindade, J.J.M. Peixoto, C.A. Silva, et al., Influence of obstruction at gas-injection nozzles (number and position) in RH degasser process, *Metall. Mater. Trans. B*, 50(2019), No. 1, p. 578.
- [19] D. Mukherjee, A.K. Shukla, and D.G. Senk, Cold model-based investigations to study the effects of operational and nonoperational parameters on the Ruhrstahl-Heraeus degassing process, *Metall. Mater. Trans. B*, 48(2017), No. 2, p. 763.
- [20] J.H. Wei and H.T. Hu, Mathematical modelling of molten steel flow in a whole degasser during RH refining process, *Ironmaking Steelmaking*, 32(2005), No. 5, p. 427.
- [21] X.G. Ai, Y.P. Bao, W. Jiang, J.H. Liu, P.H. Li, and T.Q. Li, Periodic flow characteristics during RH vacuum circulation refining, *Int. J. Miner. Metall. Mater.*, 17(2010), No. 1, p. 17.
- [22] V. Seshadri and S.L.D.S. Costa, Cold model studies of RH degassing process, *ISIJ Int.*, 26(1986), No. 2, p. 133.
- [23] Y.H. Li, Y.P. Bao, R. Wang, L.F. Ma, and J.S. Liu, Modeling study on the flow patterns of gas-liquid flow for fast decarburization during the RH process, *Int. J. Miner. Metall. Mater.*, 25(2018), No. 2, p. 153.
- [24] L. Lin, Y.P. Bao, F. Yue, L.Q. Zhang, and H.L. Ou, Physical model of fluid flow characteristics in RH-TOP vacuum refining process, *Int. J. Miner. Metall. Mater.*, 19(2012), No. 6, p. 483.
- [25] Q. Wang, S.Y. Jia, F.S. Qi, et al., A CFD study on refractory wear in RH degassing process, *ISIJ Int.*, 60(2020), No. 9, p. 1938.
- [26] B. Li and F. Tsukihashi, Modeling of circulation flow in RH degassing vessel water designed for two- and multi-legs operations, *ISIJ Int.*, 40(2000), No. 12, p. 1203.
- [27] F. Obata, R. Waka, K. Uehara, K. Ito, and Y. Kawata, Circulation characteristics of RH degassing vessel water model with multi-legs, *Tetsu-to-Hagane*, 86(2000), No. 4, p. 225.
- [28] H. Ling, L. Zhang, and C. Liu, Effect of snorkel shape on the fluid flow during RH degassing process: Mathematical modeling, *Ironmaking Steelmaking*, 45(2018), No. 2, p. 145.
- [29] T. Kuwabara, K. Umezawa, K.J. Mori, and H. Watanabe, Investigation of decarburization behavior in RH-reactor and its operation improvement, *ISIJ Int.*, 28(1988), No. 4, p. 305.
- [30] Z.F. Ren, Z.G. Luo, F.X. Meng, et al., Physical simulation on molten steel flow characteristics of RH vacuum chamber with arched snorkels, *Adv. Mater. Sci. Eng.*, 2020(2020), art. No. 6525096.
- [31] G.J. Chen and S.P. He, Mixing behavior in the RH degasser with bottom gas injection, *Vacuum*, 130(2016), p. 48.
- [32] R.D. Wang, Y. Jin, and H. Cui, The flow behavior of molten steel in an RH degasser under different ladle bottom stirring processes, *Metall. Mater. Trans. B*, 53(2022), No. 1, p. 342.
- [33] D.Q. Geng, H. Lei, and J.C. He, Simulation on flow field and mixing phenomenon in RH degasser with ladle bottom blowing, *Ironmaking Steelmaking*, 39(2012), No. 6, p. 431.
- [34] D.Q. Geng, J.X. Zheng, K. Wang, et al., Simulation on decarburization and inclusion removal process in the Ruhrstahl-Heraeus (RH) process with ladle bottom blowing, *Metall. Mater.*

- Trans. B*, 46(2015), No. 3, p. 1484.
- [35] S.P. He, G.J. Chen, and C.J. Guo, Investigation of mixing and slag layer behaviours in the RH degasser with bottom gas injection by using the VOF–DPM coupled model, *Ironmaking Steelmaking*, 46(2019), No. 8, p. 771.
- [36] J.F. Dong, C. Feng, R. Zhu, G.S. Wei, J.J. Jiang, and S.Z. Chen, Simulation and application of Ruhrstahl-Heraeus (RH) reactor with bottom-blowing, *Metall. Mater. Trans. B*, 52(2021), No. 4, p. 2127.
- [37] B. Li, Y. Luan, F. Qi, and H. Huo, Experimental investigation on circulation flow in RH refining system with swirling flow, *J. Northeast Univ.*, 26(2005), No. 8, p. 726.
- [38] B.K. Li and F. Tsukihashi, Effect of rotating magnetic field on two-phase flow in RH vacuum degassing vessel, *ISIJ Int.*, 45(2005), No. 7, p. 972.
- [39] D.Q. Geng, H. Lei, and J.C. He, Effect of traveling magnetic field on flow, mixing, decarburization and inclusion removal during RH refining process, *ISIJ Int.*, 52(2012), No. 6, p. 1036.
- [40] F.S. Qi, B.K. Li, and F. Tsukihashi, Behaviour of argon gas bubbles in an electromagnetic driven swirling flow, *Steel Res. Int.*, 78(2007), No. 5, p. 409.
- [41] L.Y. Wang, Z.Y. Liu, M. He, *et al.*, Flow fields control for bubble refinement induced by electromagnetic fields, *J. Iron Steel Res. Int.*, 29(2022), No. 4, p. 575.
- [42] W.M. Haynes, *CRC Handbook of Chemistry and Physics*, 93rd eds., CRC Press, Florida, 2012, p. 5.
- [43] J. Han, X.D. Wang, and D.C. Ba, Coordinated analysis of multiple factors of argon blowing parameters on the effect of circulation flow rate in RH vacuum refining process, *Vacuum*, 109(2014), p. 68.
- [44] COMSOL, *CFD Module User's Guide*, Release 5.3, SWE, 2017, p. 44.
- [45] B.E. Launder and D.B. Spalding, *Lectures in Mathematical Models of Turbulence*, Academic Press, New York, 1972.
- [46] COMSOL, *Particle Tracing Module User's Guide*, Release 5.6, SWE, 2020, p. 267.
- [47] Y. Luo, C. Liu, Y. Ren, and L.F. Zhang, Modeling on the fluid flow and mixing phenomena in a RH steel degasser with oval down-leg snorkel, *Steel Res. Int.*, 89(2018), No. 12, art. No. 1800048.
- [48] L. Schiller and Z.A. Naumann, A drag coefficient correlation, *Zeitschrift Des Vereins Deutscher Ingenieure*, 77(1935), p. 318.
- [49] M. Sano and K. Mori, Dynamics of bubble swarms in liquid metals, *Trans. Iron Steel Inst. Jpn*, 20(1980), No. 10, p. 668.
- [50] A. Ghaffari and A. Rahbar-Kelishami, MD simulation and evaluation of the self-diffusion coefficients in aqueous NaCl solutions at different temperatures and concentrations, *J. Mol. Liq.*, 187(2013), p. 238.